# Macroscopic Analogue to Entangled Polymers
# Supplementary Information

(Dated: April 18, 2023)

## SAMPLE PREPARATION AND IMAGING

In order to investigate the geometric and topological characteristics of disordered rubber band assemblies, we designed a straightforward experimental setup that enabled the preparation and analysis of these systems with consistent statistical properties. Our method began with the placement of rubber bands individually into a cylindrical container with a diameter of 7.5 cm. We selected the quantity of bands for each system to achieve comparable packing fractions within the volume defined by the container's dimensions.

Once the bands were in place, we mixed the system by rotating the container around an axis running through its center of mass. The mixing speed was maintained at 50 rpm for a duration of 5 minutes. This uncomplicated mixing technique resulted in disordered packings exhibiting consistent geometric and topological statistical properties.

To enhance system mixing, we utilized a container featuring a movable cap, providing the bands with a larger rotational volume. Additionally, we applied slight compression to the bands by lowering the cap to a final height of 7.2 cm. Our observations indicated that adjustments to mixing speed or duration did not significantly impact packing structure, implying a robust and dependable mixing process.

To assess the internal structures of the band packings, we employed X-ray tomography using a CT-Rex machine (Fraunhofer EZRT) situated at the Friedrich-Alexander-Universität. The X-ray source was typically set to 100 kV voltage and 350 $\mu$A current, with an exposure time of 150 ms. Tomograms were obtained by rotating the sample 1,600 times. To enhance the statistical reliability of our analysis, we imaged and examined three independent configurations for each type of band considered. With a voxel resolution of 35 $\mu$m, we were able to discern individual rubber bands and their positioning within the assembly. Figure 1 displays a representative tomogram of a structure acquired for band type $B$, which had a length of 24.1 cm and a cross-sectional area of 0.024 cm$^2$.

FIG. 1. **Raw data.** A typical tomography obtained in this work (system $B$).

## INDIVIDUAL IDENTIFICATION OF BANDS (SEGMENTATION)

Conventional 3D tomography in our project typically contains approximately 6 x $10^8$ voxels, arranged in a 3D matrix with dimensions of around 960 $x$ 960 $x$ 686. In this section, we discuss the method developed to identify each band in the assemblies from the raw data.

**Initial Binarization.** First, we remove the cylindrical container from the experimental data. A simple code enables us to manually set the axis and radius of the cylinder, clamping any value outside this geometry to zero. We then perform binarization of the 3D data, clamping any intensity below a given threshold to zero and to one otherwise. The entire volume data is binarized by slicing on the z-axis. After testing numerous schemes to determine the optimal global threshold, we found Otsu's method provides the most satisfactory results.

**Segmentation.** Segmentation typically involves separating an image into objects of interest and non-interest. In our case, we aim to distinguish each rubber band from the background and other bands. To achieve this, we first perform a distance transform on the binarized tomograms to convert bright regions into catchment basins and then apply a watershed transformation [1]. Generally, the watershed transformation is insufficient for fully segmenting bands, yielding only segments or parts of bands. In general, different band pieces must be connected in an iterative paste process to obtain the full band configurations.

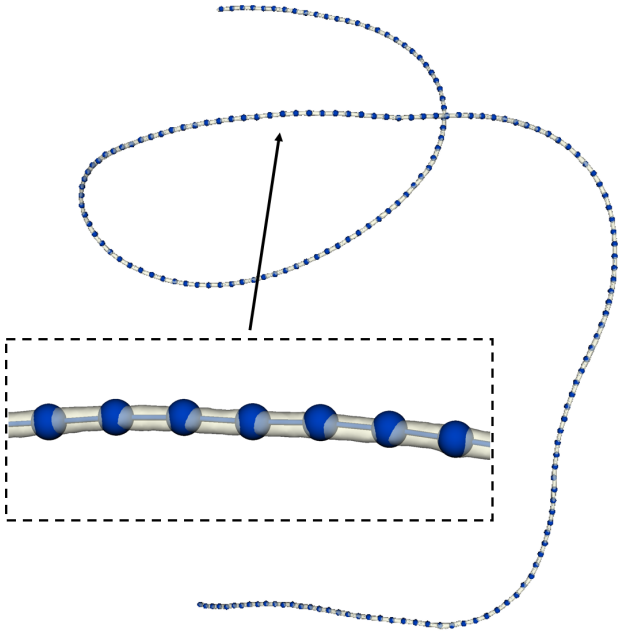

FIG. 2. **Segment skeletonization.** For a better manage the experimental data we use the skeleton transformation to replace the volumes representing the band's segments by particles chains. From the figure, it is clear that the obtained particle chains correctly locate in the middle of the bands.

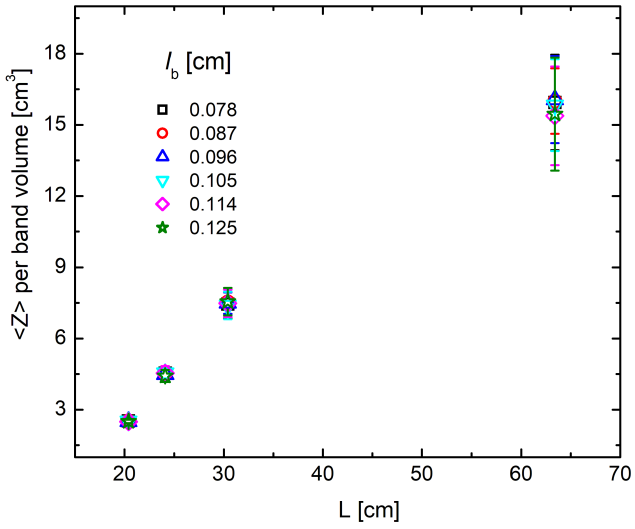


FIG. 3. **Impact of Discretization.** With sufficiently fine discretizations, the geometrical and topological properties of the bands remain unaffected by the linear chain approximation. For instance, in this plot, we illustrate the variation in entanglements within the systems for different levels of band discretization, achieved by employing various bond lengths.

In this work, we also explored a Machine Learning segmentation approach using Convolutional Neural Networks (CNNs). CNNs are a type of deep learning network designed to extract characteristic features from images and volumes [2, 3], typically through a sequence of convolution, pooling, and up-sampling operations. We employed the U-Net architecture [4] to segment the tomographies. This architecture utilizes a convolution-deconvolution approach and has been successfully applied to segmenting both 2D and 3D volumetric data [5, 6].

For our study, we trained separate U-Net networks for each type of band. The segmentation masks required to train the networks were obtained using the previously developed watershed segmentation approach [7]. For convenience, the tomograms were initially divided into subvolumes of $128^3$, and the raw data were then input to the trained network to determine the probability of a given voxel being the center of a band. After processing each subvolume, we reassembled the data in the correct order and applied a connected component analysis to obtain the individual configurations of bands. Overall, the Machine Learning segmentation approach with the U-Net CNN proved to be slightly more effective than the previous approach based on the watershed transform. Further details regarding this segmentation process will be published in a separate study.

**Discretization of bands.** To better manage the experimental data, we reduce the segmented band volume/pieces to an array of beads along its backbone using the skeleton transformation [8]. In this process, each band piece is replaced by a linear chain of particles, generally reducing a three-dimensional binary object to a 3D line one voxel wide. The algorithm is iterative, performing successive passes on the data. On each pass, border voxels of the object are identified and removed if they do not break the connectivity of the original object. We implement the algorithm reported in Ref. [9], which is designed for a 3D binary object and uses an octree data structure to examine a volume of three cubic elements surrounding a voxel. The algorithm iteratively sweeps over the image, removing voxels at each iteration until the image stops changing, at which point the process converges. Each iteration includes two steps: first, a list of candidates for removal is built; then, voxels from this list are sequentially rechecked to ensure the preservation of the object's connectivity.

While this method is versatile for processing our data and determining the backbone of the bands, it occasionally introduces spurious deviations of the band skeleton, contaminating the results. The algorithm often causes the appearance of short chains branching from the main backbone, an undesired effect related to the thickness fluctuations of the bands and a direct consequence of the binarization threshold. Consequently, we refine the skeletonization of the band by implementing an algorithm to detect and eliminate these short branches, cleaning the

trunk of the band. Figure 2 demonstrates typical discretizations of a band type $A$ obtained using our skeletonization approach.

**Iterative paste.** As mentioned earlier, the watershed segmentation generally does not fully determine band configurations but only segments or pieces of bands. Thus, a fourth step, an iterative segment-paste process, is required to obtain the full band configurations. In this step, we connect parts of bands with close endpoints and with tangent vectors at the endpoints that differ in orientation by approximately 180°. We also verify that the new bond formed (if the segments were joined) aligns with the last bonds of the chains.

To avoid misconnections, this process must be iterative. For a given distance between endpoints and a given projection of the new bond on the end-tangents, we attempt to link chains with end-tangents misoriented by approximately 180°. Once all chains are inspected, we relax the misorientation and try to link more chains. We typically progress from around 180° to approximately 60° in 20 steps. Afterward, we relax the projection of the new bond (the projection on the new bond typically decreases from 1 to 0 in 30 steps), and finally, we relax the distance between the endpoints. In each step where we try to link two chains, we also check for the length of the joined chain.

**Effects of Discretization.** It is important to note that the discretization of bands as chains of particles is entirely arbitrary, but it is extremely useful for managing data and applying different software and codes, mainly developed for the analysis of molecular dynamics simulations. In this study, we ensured that the discretization of chains was fine-grained enough so that neither geometric nor topological properties were altered. We typically employed a uniform discretization of the bands, with the bond length in the chain of the order of $l_b \sim 1mm$. This bond length was sufficiently small to yield accurate results. For instance, in Fig. 3, we display the entanglements in the different systems, as determined for six discretizations of the rubber bands. As expected, entanglements generally decrease when increasing the bond length in the approximation of the band with the chain. However, as evident from the figure, using bond lengths on the order of a millimeter ensures robust results for both geometric and topological properties.


[1] P. Acharjya, A. Sinha, S. Sarkar, S. Dey, and S. Ghosh, International Journal of Innovative Research in Computer and Communication Engineering **1**, 185 (2013).

[2] Y. LeCun, Y. Bengio, and G. Hinton, nature **521**, 436 (2015).

[3] J. Long, E. Shelhamer, and T. Darrell, in *Proceedings of the IEEE conference on computer vision and pattern recognition* (2015) pp. 3431–3440.

[4] O. Ronneberger, P. Fischer, and T. Brox, in *International Conference on Medical image computing and computer-assisted intervention* (Springer, 2015) pp. 234–241.

[5] T. Falk, D. Mai, R. Bensch, Ö. Çiçek, A. Abdulkadir, Y. Marrakchi, A. Böhm, J. Deubner, Z. Jäckel, K. Seiwald, *et al.*, Nature methods **16**, 67 (2019).

[6] Ö. Çiçek, A. Abdulkadir, S. S. Lienkamp, T. Brox, and O. Ronneberger, in *International conference on medical image computing and computer-assisted intervention* (Springer, 2016) pp. 424–432.

[7] L. R. Gómez, N. A. García, and T. Pöschel, Proceedings of the National Academy of Sciences **117**, 3382 (2020).

[8] J. Lux, Image Analysis & Stereology **32**, 13 (2013).

[9] T.-C. Lee, R. L. Kashyap, and C.-N. Chu, CVGIP: graphical models and image processing **56**, 462 (1994).